Geophys. J. Int. (This is a preprint version.) **XXX**, 1–9

Solution of the Bloch Equation Based on Spectral Diagonalization and Matrix Exponential Integration: Modeling of SSFP for SNMR

Tingting Lin, [1,2] Qingyue Wang,[1,2] Chuandong Jiang,[1,2] Chunpeng Ren,[1,2] Yunzhi Wang[1,2] and Liang Wang[3]

[1] *State Key Laboratory of Deep Earth Exploration and Imaging, College of Instrumentation and Electrical Engineering, Jilin University, Changchun,* 130026*, China. E-mail: jiangchuandong@jlu.edu.cn*

[2] *Key Laboratory of Geophysical Exploration Equipment, Ministry of Education of China, Changchun* 130026*, China*

[3] *School of Mechanical and Aerospace Engineering, Jilin University, Changchun 130025, China*

SUMMARY

We present a spectral-diagonalization-based matrix exponential integration (SD-MEI) algorithm for efficient and stable solutions of fully coupled Bloch equations in surface nuclear magnetic resonance (SNMR). Conventional explicit numerical methods exhibit cumulative discretization errors and escalating computational costs due to step-size dependence and finite precision limitations. SD-MEI integrates spectral diagonalization with matrix exponential operations, replacing iterative computations with a single eigendecomposition of the system matrix. This approach achieves parameter-robust computational complexity while maintaining numerical stability across broad RF field strengths (10^{-10} T to 10^{-5} T) and relaxation times (10 ms to 1000 ms). Validated for steady-state free precession (SSFP) dynamics in heterogeneous geomagnetic environments, the method enables high-accuracy modeling of transient magnetization evolution with large time steps. The framework advances SNMR efficient forward modeling and inversion while optimizing protocols by resolving critical limitations in existing numerical and analytical approaches.

Key words: Bloch equations; Spectral diagonalization; Matrix exponential integration.

1 INTRODUCTION

Nuclear magnetic resonance (NMR) is a spectroscopic technique that detects quantized transitions of nuclear spin energy states through resonant absorption of radiofrequency electromagnetic radiation in a static magnetic field (Bloch 1946; Purcell *et al.* 1946), with principal applications spanning molecular structure determination, material characterization, and non-invasive imaging. As a geophysical extension of NMR principles, Surface Nuclear Magnetic Resonance (SNMR) utilizes surface-deployed excitation pulses to selectively energize groundwater hydrogen nuclei(Weichman *et al.* 2000), where subsequent analysis of relaxation decay signals enables subsurface hydrogeological parameterization through multicomponent inversion (Legchenko 2004).

In contrast to laboratory NMR systems that employ precisely controlled static and radiofrequency (RF) magnetic field configurations (Bloch 1946), SNMR must account for the spatiotemporal dynamics of bulk magnetization vectors evolving under Earth's ambient geomagnetic field with inherent spatial heterogeneities (Hertrich, Braun, *et al.* 2007). This complex spin-system behavior is governed by modified Bloch equations, which mathematically formalize the interdependent dynamics between three principal mechanisms: (i) Larmor precession under non-uniform static fields, (ii) spin relaxation processes characterized by intrinsic T_1 (longitudinal) and T_2 (transverse) time constants, and (iii) nonlinear excitation effects induced by surface-deployed RF pulses (Frimmer & Novotny 2014).

Modern SNMR implementations employ three principal detection methodologies: Free Induction Decay (FID), Spin Echo (SE), and Steady-State Free Precession (SSFP) (Griffiths, D. J. Grombacher, *et al.* 2021). The SSFP technique achieves magnetization vector stabilization through precisely timed radiofrequency pulse trains, simultaneously improving the signal-to-noise ratio (SNR) via coherent signal accumulation in steady-state conditions (Grombacher *et al.* 2021). This characteristic renders SSFP particularly valuable for high-sensitivity measurements in geophysically heterogeneous magnetic environments. Nevertheless, the spatiotemporal dynamics of SSFP magnetization vectors encompass complex transient processes under field inhomogeneity effects, creating numerical challenges in Bloch equation solutions owing to both computational intensity and memory limitations.

Current Bloch equation solutions in SNMR include: (1) analytical approximations (Madhu & Kumar 1997; Miao *et al.* 2024), (2) numerical differentiation (Singh & Srivastava 2020; Griffiths, Denys Grombacher, *et al.* 2022), and (3) Laplace transforms (Bain

et al. 2010). While Hertrich et al.'s quasi-static solution (Hertrich 2008) works for short pulses by neglecting RDP effects, it fails for long or multi-pulse cases requiring precise RDP characterization (Behroozmand *et al.* 2015). The fourth-order Runge-Kutta (RK4) method solves the full Bloch equation but suffers computational inefficiency. GPU-accelerated interpolation (Denys Grombacher, Kass, *et al.* 2020) improves speed but faces memory limits and interpolation errors. Analytical approaches like Murase's matrix diagonalization (Murase & Tanki 2011) introduce 4D complexity, while Johnston's solution (Johnston 2020) is limited by its strict $B_1 > 10^{-8}T$ and $T_1 = T_2$ assumptions - conditions rarely met in SNMR's broad B_1 ranges and $T_1 \leq T_2 T$ environments.

To address these critical challenges, we propose a spectral-diagonalization-based matrix exponential integration (SD-MEI) algorithm that fundamentally transforms the paradigm for solving transient Bloch equations in SNMR applications. Departing from conventional time-domain iterative approaches, our method establishes a novel mathematical framework that leverages spectral decomposition and matrix exponential operations to convert the differential problem into an elegant linear algebraic formulation.

The SD-MEI algorithm demonstrates three key innovations: (1) it replaces computationally intensive iterative procedures with a single system matrix eigendecomposition, achieving unprecedented efficiency gains; (2) it maintains exceptional numerical stability even under challenging conditions of long-time evolution and large time steps; and (3) it provides rigorous mathematical guarantees while handling the fully coupled Bloch equations in complex, inhomogeneous field scenarios. This represents a significant theoretical and computational advancement over existing methods, offering a robust solution that simultaneously addresses the critical limitations of computational efficiency, numerical stability, and physical accuracy in SNMR forward modeling and inversion.

2 BACKGROUND AND THEORY

The surface NMR signal originates from hydrogen protons in underground aquifers. Under the Earth's magnetic field B_0, these protons precess around the field direction at the Larmor frequency $\omega_L = \gamma B_0$, forming a macroscopic equilibrium magnetization vector $\boldsymbol{M}_0$ aligned with B_0. When an alternating current with frequency ω_L is applied to the transmitting coil, the excited magnetic field B_1 tilts the equilibrium magnetization vector $\boldsymbol{M}_0$, thereby generating a transverse magnetization component $\boldsymbol{M}_\perp$. Following the pulse ends, the relaxation processes characterized by longitudinal (T_1) and transverse (T_2) relaxation times govern the gradual decay of $\boldsymbol{M}_\perp$. This time-dependent decay induces a measurable voltage signal $V(q,t)$ in the receiving coil (Weichman *et al.* 2000; Hertrich 2008). Assuming that each unit volume element $d^3\mathbf{r}$ in an underground aquifer is characterized by a water content $\mathbf{w}(\mathbf{r})$ and an exponential relaxation time $T_2^*(\mathbf{r})$, the $V(q,t)$ can be expressed as (Denys Grombacher, Walbrecker, *et al.* 2014):

$$V(q,t) = \int \mathbf{K}(q,\mathbf{r}) \cdot \mathbf{w}(\mathbf{r}) \cdot e^{-t/T_2^*(\mathbf{r})} d^3\mathbf{r} \tag{1}$$

where $V(q,t)$ is the induced voltage of pulse moment q at time t and $q = I_0 \cdot \tau$ is the product of the transmit current amplitude I_0 and the pulse duration τ. $\mathbf{K}(q,\mathbf{r})$ is referred to as the sensitivity kernel function. The amplitude of the signal generated by the aquifer is quantified when the pulse moment is q and the water content in the unit volume element at position $\mathbf{r}$ is 100%. $\mathbf{K}(q,\mathbf{r})$ is dependent on the measurement scheme and geological conditions. The kernel function of the transmitting and receiving separate coils can be expressed as follows (Hertrich, Green, *et al.* 2009):

$$\begin{aligned}\mathbf{K}(q,\mathbf{r}) = &-2\omega_L \boldsymbol{M}_0 \cdot \boldsymbol{M}_\perp(q,\mathbf{r}) \\ &\times \boldsymbol{R}_x(\mathbf{r}) \cdot e^{i[\boldsymbol{\xi}_T(\mathbf{r}) + \boldsymbol{\xi}_R(\mathbf{r})]} \\ &\times [\hat{\boldsymbol{b}}_{R\perp}(\mathbf{r}) \cdot \hat{\boldsymbol{b}}_{T\perp}(\mathbf{r}) + i\hat{\boldsymbol{b}}_0 \cdot \hat{\boldsymbol{b}}_{R\perp}(\mathbf{r}) \times \hat{\boldsymbol{b}}_{T\perp}(\mathbf{r})]\end{aligned} \tag{2}$$

where $\boldsymbol{M}_\perp(q,\mathbf{r})$ is the component of the unit magnetization intensity in the direction perpendicular to B_0. $\boldsymbol{R}_x(\mathbf{r})$ denotes the spatial sensitivity of the receiving coil. $\boldsymbol{\xi}_T(\mathbf{r})$ and $\boldsymbol{\xi}_R(\mathbf{r})$ are the phase components of the transmitting field and receiving field, respectively, under elliptical polarization (Weichman *et al.* 2000; Girard *et al.* 2005). $\hat{\boldsymbol{b}}_0$, $\hat{\boldsymbol{b}}_{R\perp}(\mathbf{r})$, and $\hat{\boldsymbol{b}}_{T\perp}(\mathbf{r})$ are the unit direction vectors for the Earth's magnetic field, transmitting field, and receiving field, respectively.

2.1 Bloch equations

Transverse magnetization $M_\perp$, as one of the critical factors influencing surface nuclear magnetic resonance (NMR) signals, plays a pivotal role in characterizing hydrogeological parameters such as water content and pore-scale properties(Mohnke & Yaramanci 2008). In practical applications, to obtain the global surface NMR response, it is necessary to solve for $M_\perp$ within each voxel of a discretized subsurface model. At the voxel scale, the dynamic evolution of nuclear magnetization in magnetic fields is governed by the Bloch equations(Bloch 1946):

$$\frac{d\boldsymbol{M}(t)}{dt} = \gamma \boldsymbol{M} \times \boldsymbol{B} - \frac{M_x}{T_2}\hat{x} - \frac{M_y}{T_2}\hat{y} - \frac{(M_z - M_0)}{T_1}\hat{z}. \tag{3}$$

where, the magnetization vector is $\boldsymbol{M}(t) = \begin{bmatrix} M_x & M_y & M_z \end{bmatrix}^{\mathrm{T}}$. The transverse components M_x and M_y (or equivalently $M_\perp = M_y + iM_x$) are independent of the longitudinal component M_z. The transverse components are spread around the z-axis and collectively decay to zero at a rate controlled by the transverse relaxation time T_2. The longitudinal component M_z undergoes exponential decay toward the equilibrium magnetization M_0, governed by the longitudinal relaxation time T_1. Typically, the transverse magnetization $M_\perp$ is modeled in a coordinate system rotating around the z-axis with the transmitter frequency ω_T.

In the rotating frame, $\boldsymbol{B}$ of eq. (3) is replaced by a $\boldsymbol{B}_{\text{eff}}$ vector:

$$\boldsymbol{B}_{\text{eff}} = \begin{bmatrix} B_1 \cos\theta & B_1 \sin\theta & \Delta/\gamma \end{bmatrix}^{\mathrm{T}}. \tag{4}$$

where θ is the phase of excitation field, and $\Delta = |\omega_L - \omega_T|$ is the instantaneous offset between the Larmor frequency ω_L and the transmit frequency ω_T. Further, the Bloch equation can be written in the following form:

$$\frac{d\boldsymbol{M}}{dt} = -\mathbf{H}\boldsymbol{M} + \begin{bmatrix} 0 \\ 0 \\ R_1 M_0 \end{bmatrix}. \tag{5}$$

where

$$\mathbf{H} = \begin{bmatrix} R_2 & -\Delta & \omega_1 \sin\theta \\ \Delta & R_2 & -\omega_1 \cos\theta \\ -\omega_1 \sin\theta & \omega_1 \cos\theta & R_1 \end{bmatrix}. \tag{6}$$

where R_1 and R_2 are the longitudinal and transverse relaxation rates in s^{-1}, and $\omega_1 = \gamma B_1$. γ is the gyromagnetic ratio, and M_0 is the equilibrium magnetization.

2.2 SD-MEI algorithm

We propose a spectral-diagonalization-based matrix exponential integration (SD-MEI) algorithm for efficient and stable solutions of fully coupled Bloch equations. The theoretical core of the method lies in utilizing the integral exponential solution form of the Bloch equation and, through spectral diagonalization, decomposing the system matrix into its eigenmatrix form. This transforms the differential equation solving process into scalar exponential operations in the eigenbasis. Specifically, we first perform matrix exponential integration on eq. (5), and then diagonalize the system matrix $\mathbf{H}$, obtaining the following form:

$$\begin{aligned}\boldsymbol{M}(t) &= \exp(-\mathbf{H}t)\left[\boldsymbol{M}(0) - \boldsymbol{M}_{\text{ss}}\right] + \boldsymbol{M}_{\text{ss}} \\ &= \mathbf{P}\exp(-\boldsymbol{\Lambda}t)\mathbf{P}^{-1}\left[\boldsymbol{M}(0) - \boldsymbol{M}_{\text{ss}}\right] + \boldsymbol{M}_{\text{ss}}.\end{aligned} \tag{7}$$

where $\mathbf{H} = \mathbf{P}\boldsymbol{\Lambda}\mathbf{P}^{-1}$, with $\boldsymbol{\Lambda} = \text{diag}(\lambda_1, \lambda_2, \lambda_3)$, and the diagonal elements of Λ are the eigenvalues of $\mathbf{H}$. Then, define the matrix $\mathbf{A} = \mathbf{P}\exp(-\boldsymbol{\Lambda}t)\mathbf{P}^{-1}$, the analytical expressions for the elements of matrix $\mathbf{A}$ can be obtained:

$$\begin{aligned}\mathbf{A} &= \mathbf{P}\begin{bmatrix}\exp(-\lambda_1 t) & & \\ & \exp(-\lambda_2 t) & \\ & & \exp(-\lambda_3 t)\end{bmatrix}\mathbf{P}^{-1} \\ &= \begin{bmatrix}A_{11}(t) & A_{12}(t) & A_{13}(t) \\ A_{21}(t) & A_{22}(t) & A_{23}(t) \\ A_{31}(t) & A_{32}(t) & A_{33}(t)\end{bmatrix}.\end{aligned} \tag{8}$$

Meanwhile, setting eq. (5) equal to 0, the steady-state magnetization vector $\boldsymbol{M}_{\text{ss}}$ is obtained as shown in eq. (9).

$$\begin{aligned}M_x(\text{ss}) &= R_1\left(\Delta\omega_1\cos\theta - R_2\omega_1\sin\theta\right)M_0/D \\ M_y(\text{ss}) &= R_1\left(R_2\omega_1\cos\theta + \Delta\omega_1\sin\theta\right)M_0/D. \\ M_z(\text{ss}) &= R_1\left(R_2^2 + \Delta^2\right)M_0/D\end{aligned} \tag{9}$$

where $D = R_1R_2^2 + R_1\Delta^2 + R_2\omega_1^2$. By simultaneously solving eq. (7) to eq. (9), the analytical expression for the magnetization vector $\boldsymbol{M}(t)$ at any time t is ultimately obtained, as shown in eq. (10). Through the above steps, given an initial magnetization vector $\boldsymbol{M}(0)$, the SD-MEI algorithm can efficiently solve for the magnetization vector $\boldsymbol{M}(t)$ at any time t.

$$\begin{aligned}M_x(t) =& A_{11}(t)\left[M_x(0) - M_x(\text{ss})\right] + A_{12}(t)\left[M_y(0) - M_y(\text{ss})\right] \\ &+ A_{13}(t)\left[M_z(0) - M_z(\text{ss})\right] + M_x(\text{ss}) \\ M_y(t) =& A_{21}(t)\left[M_x(0) - M_x(\text{ss})\right] + A_{22}(t)\left[M_y(0) - M_y(\text{ss})\right] \\ &+ A_{23}(t)\left[M_z(0) - M_z(\text{ss})\right] + M_y(\text{ss}) \\ M_z(t) =& A_{31}(t)\left[M_x(0) - M_x(\text{ss})\right] + A_{32}(t)\left[M_y(0) - M_y(\text{ss})\right] \\ &+ A_{33}(t)\left[M_z(0) - M_z(\text{ss})\right] + M_z(\text{ss})\end{aligned} \tag{10}$$

2.3 Implementation of spectral diagonalization

In the SD-MEI algorithm, the spectral diagonalization of the system matrix $\mathbf{H}$ is a core step for achieving high-precision solutions. Considering that the system matrix $\mathbf{H}$ in the Bloch equation exhibits quasi-Hermitian properties, this study adopts a hybrid diagonalization strategy that combines Hessenberg preprocessing with implicit double-shift QR iteration. Specifically, the Hessenberg transformation is first applied to convert $\mathbf{H}$ into an upper Hessenberg matrix, reducing the computational complexity of QR iterations from $O(n^3)$ to $O(n^2)$. Next, Wilkinson's double-shift strategy is introduced to enhance convergence efficiency. At the same time, the implicit QR iteration is employed to avoid the numerical instability that could arise from explicit matrix power operations. This method is consistent with the implementation mechanism of MATLAB's eig function and ensures high-precision diagonalization even under non-Hermitian structures.

Table 1. Parameter settings of the system matrix $\mathbf{H}$ in the Bloch equation model based on SNMR.

Continuous Variables	**Value Range**	
	MIN	**MAX**
T_1 (ms)	10	1000
T_2 (ms)	10	1000
B_1 (T)	10^{-10}	10^{-5}
Δ (rad/s)	-100	100
Discrete Variables	**Value Options**	
θ	$0°, 90°$	

To assess the numerical accuracy of the `eig` function in MATLAB during spectral diagonalization, we performed numerical experiments on the system matrix $\mathbf{H}$. The parameters used in the experiments reflect typical values encountered in practical applications, as summarized in Table 1. The diagonalization accuracy was evaluated by computing the Frobenius norm error. The experimental procedure is outlined as follows:

- Perform spectral decomposition on the system matrix $\mathbf{H}$:

$$[\mathbf{P}, \boldsymbol{\Lambda}] = \texttt{eig}(\mathbf{H})$$

- Reconstruct the system matrix $\mathbf{H}_{\text{re}}$ using:

$$\mathbf{H}_{\text{re}} = \mathbf{P}\boldsymbol{\Lambda}\mathbf{P}^{-1}$$

- Compute the Frobenius norm error (F-norm) of the system matrix reconstruction:

$$\|\mathbf{H} - \mathbf{H}_{\text{re}}\|_F$$

We numerically evaluated the spectral diagonalization accuracy of the system matrix $\mathbf{H}$ under two conditions: zero frequency offset ($\Delta = 0$ rad/s) and multiple frequency offsets ($\Delta \in [-100, 100]$ rad/s). First, numerical experiments were performed under zero frequency offset conditions ($\Delta = 0$ rad/s), with the B_1 field sampled at 101 logarithmically spaced points from 10^{-10} T to 10^{-5} T. The relaxation times T_1 and T_2 were each sampled uniformly at 34 points over the range of 10 ms to 1000 ms. Subsequently, multi-frequency offset experiments were conducted with B_1 fixed at three representative values: 10^{-10} T, 10^{-7} T, and 10^{-5} T. The frequency offset Δ was sampled uniformly at 51 points within the range of -100 rad/s to 100 rad/s, while the other parameters were kept unchanged.

As shown in Fig. 1, under the zero frequency offset condition, the F-norm error exhibits a slow upward trend as B_1 increases, with a maximum F-norm error below 10^{-11} (Fig. 1 (a)). This is attributed to the increase in the magnitude of off-diagonal elements of $\mathbf{H}$ as ω_1 grows, which reduces the stability of eigenvector reconstruction. However, due to the numerical stability of the QR method, the overall F-norm error remains at a negligible

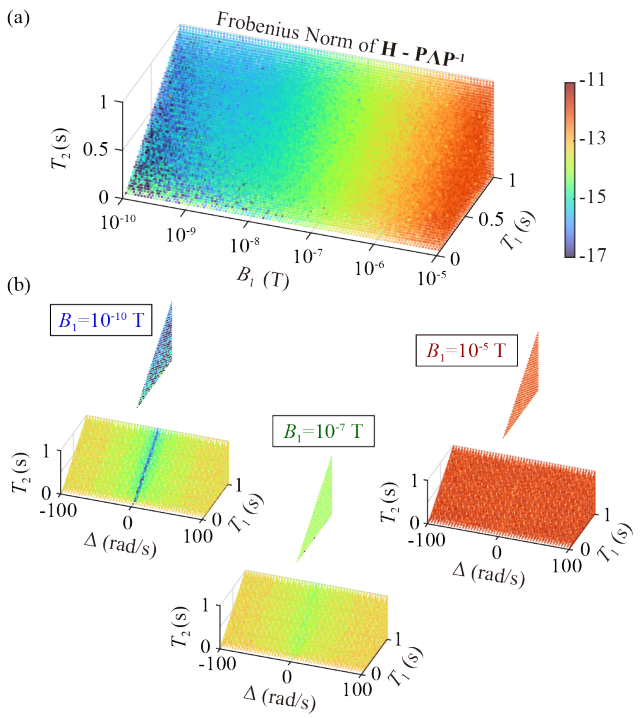

Figure 1. Frobenius norm errors of the spectral diagonalization of the system matrix $\mathbf{K}$. (a) Errors under the zero frequency offset condition with $\Delta = 0$ rad/s. (b) Errors under multi-frequency offset conditions with $\Delta \in [-100, 100]$ rad/s. In both cases, the maximum Frobenius norm error remains within the order of 10^{-11}, demonstrating the high numerical stability of the eigen decomposition.

level. Under multiple frequency offset conditions (Fig. 1 (b)), the F-norm error increases with $|\Delta|$, indicating that frequency offsets enhance the non-Hermitian characteristics of the system, perturbing the eigenstructure and increasing spectral reconstruction error. Nevertheless, the maximum F-norm error remains within the order of 10^{-11}, demonstrating strong robustness.

We further analyze the implications of spectral decomposition on the computation of the matrix exponential $\exp(\mathbf{H})$. Given the reconstruction $\mathbf{H}_{\text{re}}$ with:

$$\|\mathbf{H}_{\text{re}} - \mathbf{H}\|_F \leq \epsilon. \tag{11}$$

Considering that the matrix exponential is Lipschitz continuous in the Frobenius norm, we have:

$$\|\exp(\mathbf{H}_{\text{re}}) - \exp(\mathbf{H})\|_F \leq C\epsilon. \tag{12}$$

where C is a constant determined by the spectral norm of $\mathbf{H}$. Since ε is on the order of 10^{-11}, the error in the matrix exponential remains within the same magnitude, ensuring sufficient accuracy for high-fidelity simulations.

3 NUMERICAL EXPERIMENTS

To systematically evaluate the performance of the SD-MEI algorithm in SNMR applications, we conducted comprehensive validation from three key perspectives: magnetization vector accuracy, computational efficiency, and forward modeling capability. The experiments were designed to rigorously assess the algorithm's robustness under both standard and extreme parameter configurations. For the commonly used detection sequences—Free Induction Decay (FID), Spin Echo (SE), and Steady-State Free Precession (SSFP)—we selected parameter ranges for the system matrix $\mathbf{H}$ that align with practical application requirements, as summarized in Table 1. To provide a high-precision benchmark, we adopted the RK4 numerical solution, implemented using MATLAB's ode45 solver with adaptive step-size control. The solver's relative and absolute error tolerances were both set to 10^{-12}, ensuring reference-level accuracy for comparative analysis.

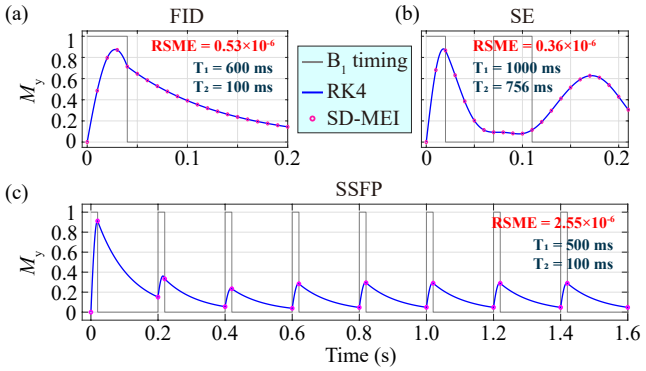

Figure 2. Comparison of magnetization vector evolution trajectories between SD-MEI and RK4 algorithm. The blue solid line represents the magnetization vector computed using the RK4 method, while the purple circles indicate the results obtained from the SD-MEI method. (a) Comparison of FID sequences and (b) Comparison of SE sequences, both solved with a fixed time step of $\Delta t = 10$ ms; (c) Comparison of SFFP sequences, where the time step is determined based on the RF excitation duration and relaxation time, with magnetization states computed only at the end of excitation and the start of the next excitation.

3.1 Magnetization vector

3.1.1 Typical SNMR pulse sequences

To assess the precision of the SD-MEI algorithm in capturing the magnetization vector evolution, we consider three classical SNMR pulse sequences: FID, SE, and SSFP. The simulated trajectories of magnetization vectors using SD-MEI are compared to those obtained from the RK4 method. Results are illustrated in Fig. 2, the magnetization trajectories computed by SD-MEI exhibit excellent agreement with those derived from the RK4 method across all three pulse sequences, indicating the high numerical precision and stability of the proposed algorithm. Quantitatively, the root mean square errors (RMSE) between SD-MEI and RK4 results are 0.53×10^{-6} for the FID sequence, 0.36×10^{-6} for the SE sequence, and 2.55×10^{-6} for the SSFP sequence. These results confirm the reliability and robustness of the SD-MEI algorithm under different SNMR excitation conditions, with all RMSE values reaching the order of 10^{-6}.

Notably, the SD-MEI algorithm is independent of the evolution time t, enabling flexible computation of the magnetization state at arbitrary time points—such as the moment immediately following RF excitation. Specifically, for the FID and SE sequences (Fig. 2 (a) and Fig. 2 (b)), simulations are conducted with a fixed time step of $\Delta t = 10$ ms. In contrast, for the SSFP sequence (Fig. 2 (c)), the time step is adjusted based on the RF excitation duration and relaxation times. The magnetization vector is computed only at key time points, namely, at the end of each excitation and the beginning of the next.

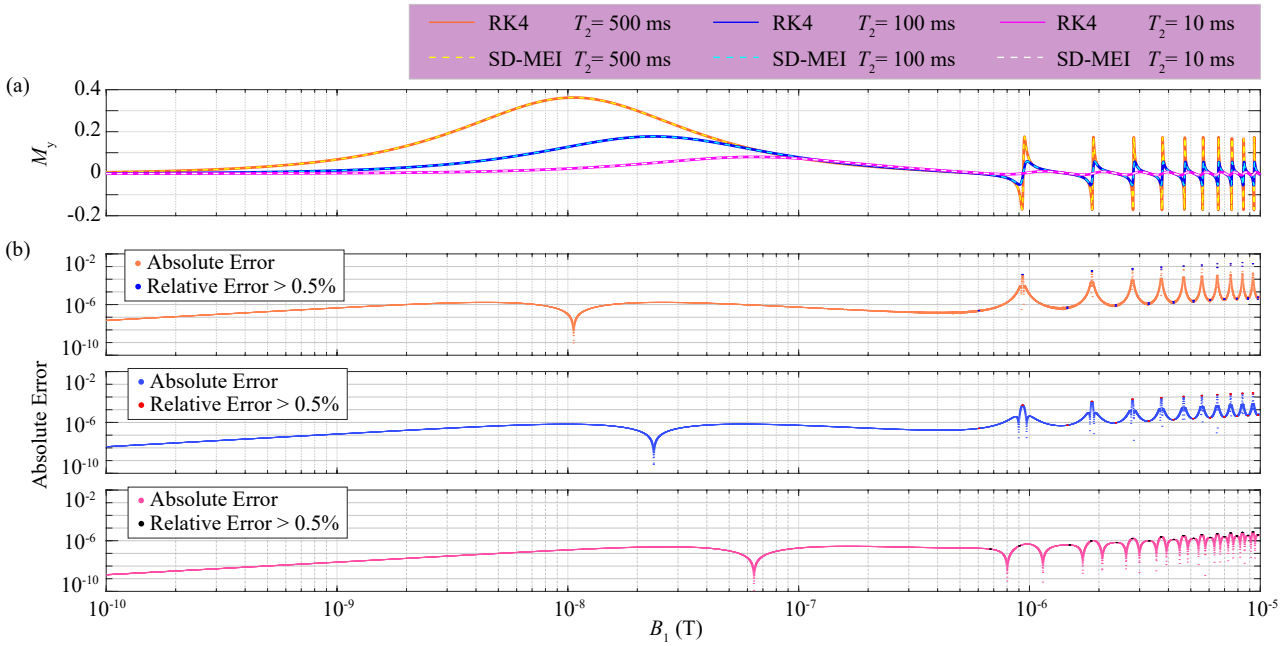

Figure 3. Evolution of M_y under different transverse relaxation times T_2 (500 ms, 100 ms, 10 ms). (a) Evolution of M_y as a function of B_1 field strength when SSFP reaches a steady state. (b) Absolute error (AE) between the SD-MEI solution and the RK4 reference solution for different T_2 values, with parameter points where the relative error (RE) exceeds 0.5% specifically highlighted.

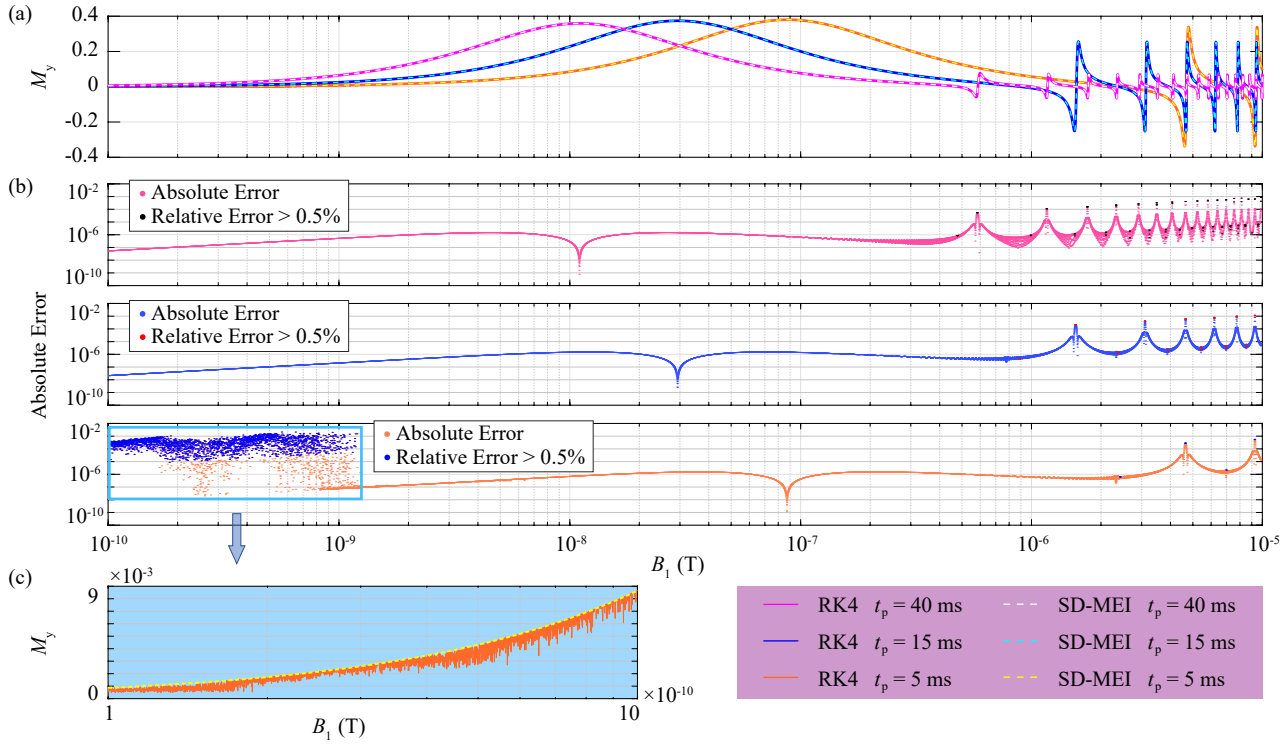

Figure 4. Evolution of M_y under different excitation durations (τ = 5 ms, 15 ms, 40 ms) with a fixed excitation period (t_{rep}) of 50 ms. (a) Evolution of M_y as a function of B_1 field strength when SSFP reaches a steady state. (b) Absolute error between the SD-MEI solution and the RK4 reference solution for different τ values, with parameter points where the relative error (RE) exceeds 0.5% specifically highlighted. (c) Evolution of the SD-MEI solution and the RK4 reference solution under weak excitation field($B_1 < 10^{-9}$ T) conditions for τ = 5 ms.

3.1.2 Steady-state free precession

To verify the universality and stability of the SD-MEI algorithm in complex sequences, additional validation experiments were conducted using the SSFP sequence as the subject of study. Fig. 3 (a) reveals the dynamic response of the steady-state transverse magnetization component M_y as the B_1 field strength varies under different T_2 conditions (T_2=500 ms, 100 ms, and 10 ms). Quantitative analysis in Fig. 3 (b) demonstrates that the SD-MEI algorithm maintains consistent solving stability across six orders of B_1 field magnitude, with absolute error (AE) relative to the RK4 reference solution generally remaining below the 10^{-4} level. Notably, 99.6% of data points exhibit a relative error (RE) below 0.05%, strongly demonstrating the algorithm's computational accuracy advantage across a wide parameter range.

Furthermore, Fig. 4 presents the magnetization response characteristics under different excitation pulse widths (τ = 5 ms, 15 ms, 40 ms) when the period is fixed at 50 ms. Experimental results (Fig. 4 (a)-(b)) indicate that, under varying τ conditions, the SD-MEI algorithm maintains high consistency with the RK4 reference solution. Especially under extreme conditions of ultra-weak field strength ($B_1 < 10^{-9}$ T) and short excitation duration (τ = 5 ms), the solution curve obtained by SD-MEI exhibits superior smoothness and remains physically consistent (Fig. 4 (c)). In contrast, the conventional explicit RK4 integrator suffers from computational deviations due to the failure of its adaptive step-size mechanism and floating-point precision limitations, resulting in significant oscillatory behavior in the solution.

A comprehensive analysis of the error distributions in Fig. 3 (b) and Fig. 4 (b) demonstrates an increasing proportion of sampling points exceeding 0.05% RE with B_1 field strength amplifies. This phenomenon arises from enhanced RF-relaxation nonlinear coupling at stronger fields, exacerbating numerical instability in conventional explicit integrators.

3.2 Computational efficiency

To comprehensively evaluate algorithm performance, we conducted a computational efficiency comparison between the proposed SD-MEI and the classical RK4 method under a single-threaded execution environment. The results, summarized in Table 2, clearly demonstrate the superior computational performance of SD-MEI, particularly for long-duration and complex pulse sequences such as SSFP. In these cases, SD-MEI achieves a speedup of 10 to 50 times compared to RK4. For example, in the SE sequence involving 501 frequency offset sampling points, SD-MEI completes the computation in 1.39 seconds, whereas RK4 requires over 56 seconds—yielding a 39-fold acceleration. Notably, for the SSFP sequence with increasing excitation field strength (B_1), the computation time of SD-MEI remains nearly constant, while that of RK4 increases significantly. This is attributed to the fact that the real-time computational complexity of SD-MEI is independent of B_1, whereas the local truncation error of RK4 scales proportionally with ${B_1}^5$. To maintain numerical accuracy, RK4 thus necessitates progressively smaller time steps under high field strengths, leading to a rapid increase in computation time.

These findings highlight the significant advantages of the SD-MEI algorithm in scenarios requiring high-throughput computation, extensive parameter sweeps, or real-time control. Its robustness to varying B_1 values and insensitivity to sequence duration make it well-suited for large-scale or time-critical SNMR simulations.

3.3 Forward modeling

To evaluate the accuracy of the SD-EMI algorithm in forward modeling, this study conducted a comparative analysis of the kernel function $\mathbf{K}$ and the steady-state induced voltage e_0 within the SSFP sequence framework. First, under four different parameter configurations, the numerical error in the kernel function $\mathbf{K}$ computed by the SD-EMI and RK4 methods was compared. As shown in Fig. 5, the absolute error between the two methods remained consistently at the picovolt (pV) level and within the order of 10^{-4}, demonstrating the high accuracy of the SD-EMI algorithm in computing kernel functions.

Furthermore, to assess the predictive capability of the SD-EMI algorithm for e_0, forward simulations were performed for various subsurface water-bearing models. For the single-layer structure (Fig. 6 (a)), three water-bearing layers were configured at shallow (5 m–8 m), intermediate (13 m–20 m), and deep (29 m–43 m) depths. The resulting e_0–q response curves obtained using SD-EMI and RK4 methods showed excellent agreement. This analysis was further extended to multilayer models (Fig. 6 (b)), where both methods again produced highly consistent results. Quantitative error analysis revealed absolute errors at the sub-picovolt level (< 1 pV) and relative errors on the order of 10^{-5}, confirming the robustness of the method in modeling complex hydrological structures.

In summary, the results demonstrate that the SD-EMI algorithm achieves microvolt-level accuracy in predicting response signals within SSFP-based forward modeling. Its close agreement with the RK4 method at the pV-level further underscores the algorithm's reliability for high-precision simulations in hydrological modeling applications.

4 DISCUSSION

The proposed SD-MEI algorithm demonstrates significant advantages in theoretical formulation, numerical stability, and adaptability to forward modeling. Building on this foundation, this section further explores the algorithm from three perspectives: algorithmic characteristics, extensibility of inversion strategies, and feasibility of engineering deployment.

First, from a structural standpoint, the SD-MEI algorithm is built upon an analytical framework designed for solving magnetization vector evolution problems. Although it adopts a closed-form solution at the global level, the spectral diagonalization of the system matrix employs numerical fitting techniques (e.g., approximate eigen-decomposition) to enhance computational efficiency and accommodate high-dimensional scenarios. Consequently, the method can be classified as "semi-analytical," representing a hybrid structure that combines analytical expressions with numerical approximations. A key evaluation metric is the error introduced during diagonalization. By assessing the reconstruction error of the system matrix using the Frobenius norm, we observe that the error consistently remains below the 10^{-11} threshold—significantly lower than typical convergence criteria in engineering optimization (ranging from 10^{-6} to 10^{-8}). This indicates that the numerical approximation closely approximates the true analytical solution, thereby preserving both the theoretical integrity and practical relevance of the method.

Secondly, the SD-MEI algorithm demonstrates significant advantages in inversion applications for groundwater detection. Compared to traditional numerical integration methods such as RK4, SD-MEI offers higher computational efficiency and stability, en-

Table 2. Comparison of computational efficiency between SD-MEI and RK4 algorithms in single-thread mode.

Sequence	Parameters			Sequence Duration (s)	Computation Time (s)		Speedup
	θ	B_1 (T)	Δ (rad/s)		RK4	SD-MEI	
FID	0°	2×10^{-7}	0	0.2	0.144	0.044	**3**
SE	0°, 90°	2.93×10^{-7}	−100 – 100 (501 sampling points)	0.21	56.047	1.390	**39**
		2.93×10^{-8}			0.401	0.031	**13**
SSFP	0°	2.93×10^{-7}	0	4	0.570	0.032	**18**
		2.93×10^{-6}			1.646	0.034	**48**

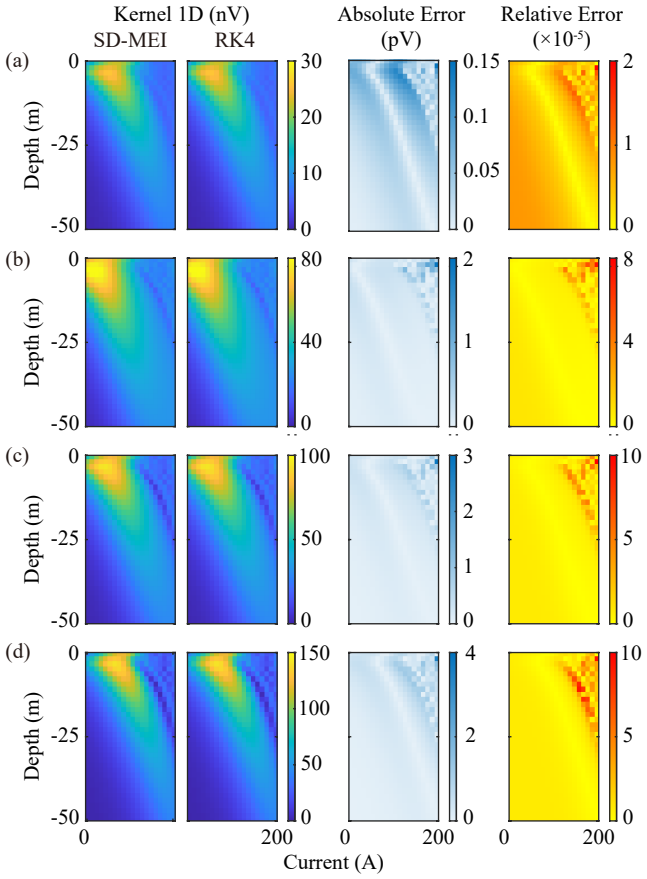

Figure 5. Quantitative evaluation of the kernel function $\mathbf{K}$ using the SD-MIE algorithm and the RK4 algorithm. (a) $\tau = 20$ ms - $t_{\text{rep}} = 100$ ms, $T_1 = 1000$ ms, $T_2 = 10$ ms. (b) $\tau = 20$ ms - $t_{\text{rep}} = 100$ ms, $T_1 = 600$ ms, $T_2 = 300$ ms. (c) $\tau = 20$ ms - $t_{\text{rep}} = 200$ ms, $T_1 = 600$ ms, $T_2 = 300$ ms; (d) $\tau = 20$ ms - $t_{\text{rep}} = 200$ ms, $T_1 = 200$ ms, $T_2 = 200$ ms.

abling reduced computational cost without compromising inversion accuracy. In challenging scenarios characterized by strong non-uniqueness and high noise levels, SD-MEI delivers more stable and reliable solutions. Furthermore, its closed-form structure yields well-behaved, differentiable response functions, which enhance convergence and improve parameter estimation accuracy—especially under complex pulse sequences like the SSFP. These features make SD-MEI a powerful tool for developing efficient and robust inversion systems for groundwater exploration, with strong potential for practical deployment.

Finally, the SD-MEI algorithm exhibits significant advantages in both computational efficiency and hardware independence. Traditional numerical integration schemes such as RK4 typically rely on small time steps and extensive iterative procedures, resulting in high computational cost and limited scalability. Although GPU-accelerated interpolation methods (Denys Grombacher, Kass, *et al.* 2020) can achieve substantial speed improvements, they require GPU hardware and preconstructed interpolation databases, leading to large memory overhead and increased system complexity. In contrast, SD-MEI employs a closed-form structure that supports large time-step updates, significantly reducing the number of iterations and intermediate computations. It maintains low memory usage and operates efficiently on standard CPUs, without the need for dedicated GPUs or large storage resources. These characteristics make SD-MEI particularly well-suited for field applications with constrained hardware conditions, and its ease of deployment further highlights its practical value and portability.

In summary, the SD-MEI algorithm closely approximates an analytical formulation in its numerical structure, offering strong mathematical rigor and practical scalability. Its compatibility with modern inversion methodologies and low-power hardware architectures provides a solid foundation for developing efficient, robust, and embeddable real-time NMR detection systems.

5 CONCLUSION

Experimental validation confirms that the SD-MEI algorithm achieves high consistency with the classical RK4 numerical solution in terms of accuracy, while demonstrating significant advantages in computational efficiency and algorithmic robustness. Particularly in long-duration and complex sequences such as SSFP, it provides crucial technical support for real-time sequence optimization and signal detection. Under ultra-weak RF field conditions ($B_1 < 10^{-9}$ T), conventional iterative methods commonly suffer from divergence issues. In contrast, the SD-MEI algorithm effectively avoids such instability, significantly reducing accuracy distortion risks in deep, high-resolution detection. Its core strength lies in the construction of an efficient algebraic reconstruction approach based on a matrix closed-form solution, coupled with a separation mechanism for the RF-relaxation matrix to effectively suppress parameter coupling effects.

By establishing a general-purpose numerically decoupled solution framework, the SD-MEI algorithm achieves critical advancements in the following aspects: (1) Modeling of Magnetization Dynamics: Accurately characterizes magnetization vector dynamics across a broad RF field strength range (10^{-10} to 10^{-5} T); (2) Control of Computational Complexity: Maintains stable computational complexity regardless of variations in the scale of physical parameters; (3) Improved Numerical Stability: Effectively addresses convergence challenges faced by conventional explicit integrators in

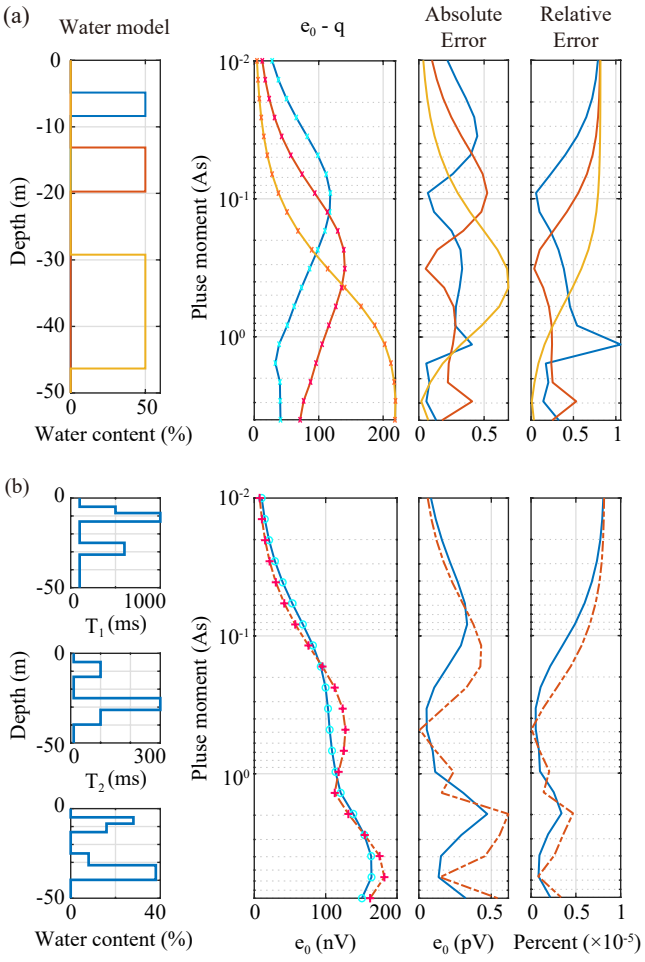

Figure 6. Quantitative evaluation of the e_0 - q response curves obtained using the SD-EMI algorithm and the RK4 algorithm. The point markers indicate the results of the SD-EMI algorithm, while solid lines represent the results of the RK4 algorithm. (a) Single-layered aquifer structure with three aquifer zones located at shallow (5–8 m), middle (13–20 m), and deep (29–43 m) depths. The simulation parameters are set as $\tau = 20$ ms, $t_{\text{rep}} = 100$ ms, with $T_1 = 600$ ms and $T_2 = 300$ ms; (b) Multi-layered aquifer structure. Two groups of response curves are shown under the same excitation time (τ) but different repetition times (t_{rep}): the blue curves correspond to $\tau = 20$ ms, $t_{\text{rep}} = 100$ ms; the red curves correspond to $\tau = 20$ ms, $t_{\text{rep}} = 200$ ms.

stiff and highly nonlinear systems; (4) Temporal Flexibility: Enables analytical computation of magnetization vectors at arbitrary time points given initial conditions, with the overall accuracy unaffected by sampling interval. In conclusion, the SD-MEI algorithm offers substantial value for real-time SNMR inversion. It not only enhances detection efficiency and interpretative reliability in complex geological environments but also establishes a solution framework that combines theoretical rigor with practical engineering applicability.

ACKNOWLEDGMENTS

This work was supported by the National Natural Science Foundation of China under Grant 42474110.

DATA AVAILABILITY

The data that support the findings of this study are available from the corresponding author upon reasonable request.

References

Bain, Alex D, Christopher Kumar Anand, & Zhenghua Nie (2010). “Exact solution to the Bloch equations and application to the Hahn echo”. In: *Journal of Magnetic Resonance* 206.2, pp. 227–240.

Behroozmand, Ahmad A, Kristina Keating, & Esben Auken (2015). “A review of the principles and applications of the NMR technique for near-surface characterization”. In: *Surveys in geophysics* 36, pp. 27–85.

Bloch, Felix (1946). “Nuclear induction”. In: *Physical review* 70.7-8, p. 460.

Frimmer, Martin & Lukas Novotny (2014). “The classical Bloch equations”. In: *American Journal of Physics* 82.10, pp. 947–954.

Girard, Jean-Francois, Anatoly Legchenko, & Marie Boucher (2005). “Stability of MRS signal and estimation of data quality”. In: *Near Surface Geophysics* 3.3, pp. 187–194.

Griffiths, Matthew P, Denys Grombacher, Lichao Liu, Mathias Ø Vang, & Jakob Juul Larsen (2022). “Forward modeling steady-state free precession in surface NMR”. In: *IEEE Transactions on Geoscience and Remote Sensing* 60, pp. 1–10.

Griffiths, Matthew P, Denys J Grombacher, & Jakob Juul Larsen (2021). “Efficient numerical Bloch solutions for multipulse surface NMR”. In: *Geophysical Journal International* 227.3, pp. 1905–1916.

Grombacher, D, L Liu, MP Griffiths, MØ Vang, & JJ Larsen (2021). “Steady-state surface NMR for mapping of groundwater”. In: *Geophysical Research Letters* 48.23, e2021GL095381.

Grombacher, Denys, Mason Andrew Kass, Esben Auken, & Jakob Juul Larsen (2020). “An approximate fast-mapping approach to the surface NMR forward problem”. In: *Geophysical Journal International* 221.2, pp. 928–937.

Grombacher, Denys, Jan O Walbrecker, & Rosemary Knight (2014). “Imparting a phase during excitation for improved resolution in surface nuclear magnetic resonance”. In: *Geophysics* 79.6, E329–E339.

Hertrich, Marian (2008). “Imaging of groundwater with nuclear magnetic resonance”. In: *Progress in Nuclear Magnetic Resonance Spectroscopy* 53.4, pp. 227–248.

Hertrich, Marian, Martina Braun, Thomas Gunther, Alan G Green, & Ugur Yaramanci (2007). “Surface nuclear magnetic resonance tomography”. In: *IEEE Transactions on Geoscience and Remote Sensing* 45.11, pp. 3752–3759.

Hertrich, Marian, Alan G Green, Martina Braun, & Ugur Yaramanci (2009). “High-resolution surface NMR tomography of shallow aquifers based on multioffset measurements”. In: *Geophysics* 74.6, G47–G59.

Johnston, Eric R (2020). “Solution of the Bloch equations including relaxation”. In: *Concepts in Magnetic Resonance Part A* 2020.1, p. 8819956.

Legchenko, Anatoli (2004). “Magnetic resonance sounding: Enhanced modeling of a phase shift”. In: *Applied Magnetic Resonance* 25.3, pp. 621–636.

Madhu, PK & Anil Kumar (1997). "Bloch equations revisited: New analytical solutions for the generalized Bloch equations". In: *Concepts in Magnetic Resonance: An Educational Journal* 9.1, pp. 1–12.

Miao, Ruixin, Yunzhi Wang, Qingyue Wang, Yan Zheng, Xiyu He, Chunpeng Ren, & Chuandong Jiang (2024). "Forward modeling of single-sided magnetic resonance and evaluation of T2 fitting error based on geometric analytical method". In: *Computers & Geosciences* 192, p. 105705.

Mohnke, O & U Yaramanci (2008). "Pore size distributions and hydraulic conductivities of rocks derived from magnetic resonance sounding relaxation data using multi-exponential decay time inversion". In: *Journal of Applied Geophysics* 66.3-4, pp. 73–81.

Murase, Kenya & Nobuyoshi Tanki (2011). "Numerical solutions to the time-dependent Bloch equations revisited". In: *Magnetic resonance imaging* 29.1, pp. 126–131.

Purcell, Edward M, Henry Cutler Torrey, & Robert V Pound (1946). "Resonance absorption by nuclear magnetic moments in a solid". In: *Physical review* 69.1-2, p. 37.

Singh, Harendra & HM Srivastava (2020). "Numerical simulation for fractional-order Bloch equation arising in nuclear magnetic resonance by using the Jacobi polynomials". In: *Applied Sciences* 10.8, p. 2850.

Weichman, Peter B, Eugene M Lavely, & Michael H Ritzwoller (2000). "Theory of surface nuclear magnetic resonance with applications to geophysical imaging problems". In: *Physical Review E* 62.1, p. 1290.